Concepts and Properties of Controlled Permanent Magnet Drives

C. Grabner

Abstract — The considered converter-fed permanent magnet motor could alternatively be operated in two basically different states – the vector control mode or alternatively the brushless dc, also known as electronically commutated mode. Several quality aspects concerning the system performance have been comparatively investigated in practical as well as theoretical manner. Focus is thereby given to the numerical analysis and previous evaluation of the well interaction between the novel axially un-skewed higher harmonic air-gap wave based permanent magnet motor design and both completely different control algorithms.

I. INTRODUCTION

A straightforward industrial development process of electrical variable speed drive systems is fortunately assisted by modern commercial calculation tools [1-3]. However, the extensive and almost precise analysis of the interaction of different control algorithms, like the vector control or the brushless DC mode, within introduced innovative permanent magnet motor topologies, as e.g. the higher harmonic air-gap based design, is still a big challenge [4-6]. The implemented main software features, the interacting converter hardware and the motor itself are almost analyzed in the time-domain.
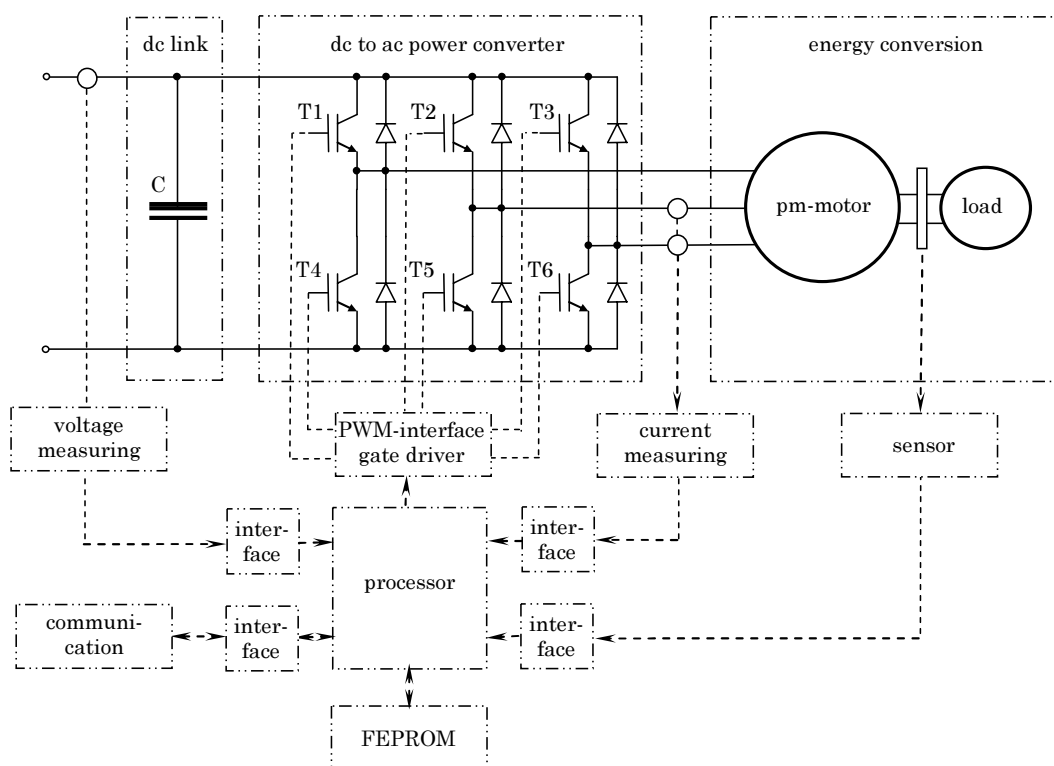

Figure 1. Outline of important devices of the considered drive system.

II. REALIZED DRIVE SYSTEM

The investigated drive system is made up of many different hardware components [7-9]. The essential internal interaction between the supply dc-link, the dc to ac power converter, the motor, the sensor, the controllers and communicating tasks is schematically depicted in Fig.1. The power conversion from the constant dc voltage link level to the ac voltage system at the motor is elementary performed by the PWM technology. The motor construction itself is built up for a mechanical rated load of approximately 1.35 Nm. Depending on the control mode, an encoder or Hall-sensor is used. The communication purposes as well as main current and speed control algorithm are implemented in the processor.

III. HIGHER HARMONIC AIR-GAP WAVE BASED PERMANENT MAGNET MOTOR DESIGN

The moving rotor with attached permanent magnets is almost characterized by its even number of involved magnetic poles, whereas the fixed novel stator winding design comprises the same pole number by means of higher space harmonics [10]. Both, stator and rotor designs are unskewed.
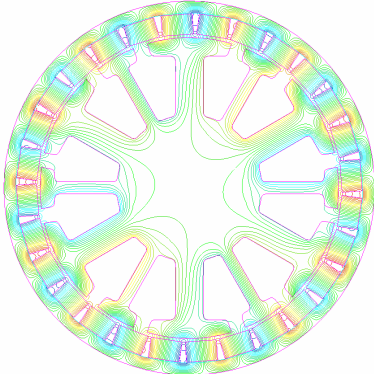

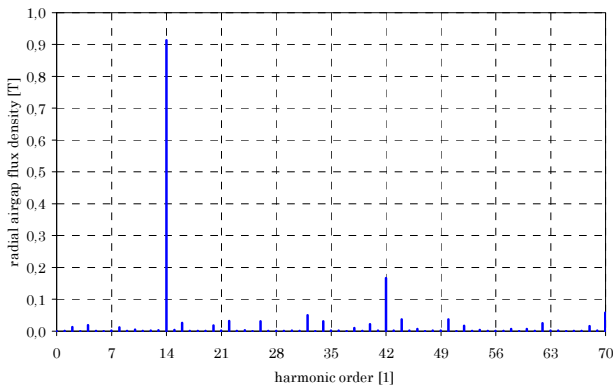Figure 2. Constant magnetic vector potential lines at no-load for the range ±0.002 Vs/m.

Figure 3. Fourier spectrum $\hat{B}_k$ of the radial flux density component at no-load.

A. Design of the permanent magnet rotor

Obviously a number of $p = 14$ magnetic pole pairs are generated along the circumferential air gap direction. Favorably, the high pole number allows a very thin yoke construction. The invoked distribution of the magnetic field due to permanent magnet excitation is shown in Fig.2. The series space expansion of the radial flux density component $B_r(\varphi)$ in accordance to

$$B_r(\varphi) = \sum_{k=0}^{\infty} \hat{B}_k \sin\left(k \cdot \frac{\varphi}{2\pi} + \alpha_k\right) \qquad (1)$$

yields several harmonic coefficients $\hat{B}_k$, $k \in \mathbb{N}$ with some distinct contributions, as it is obvious from Fig.3. The fourteenth component $\hat{B}_{14} = 0.91\,\text{T}$ in the no-load spectrum acts thereby as the fundamental air-gap wave of the drive.

B. Stator design invoking distinct harmonics

In order to generate the same number of $p = 14$ rotor pole pairs, a fourteenth harmonic wave in the circumferential air gap flux density distribution has to be generated from the stator current excitation. This is advantageously done by the established alternating thin and thick tooth structure along the circumferential air gap.
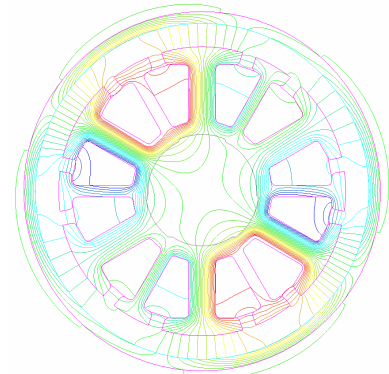

Figure 4. Constant magnetic vector potential lines in case of stator current injection for the range ±0.002 Vs/m.
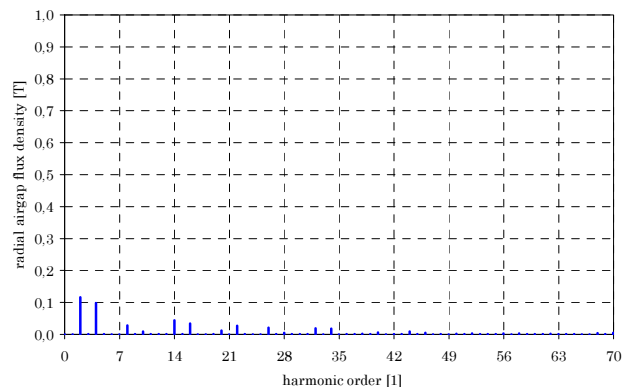

Figure 5. Fourier spectrum $\hat{B}_k$ of the radial flux density component at default stator current.

The numerically calculated distribution of the magnetic field due to the stator current excitation only is shown in Fig.4. From the series expansion (1), the harmonic components $\hat{B}_k$, $k \in \mathbb{N}$ of the wide spectrum in Fig.5 are obtained. There exists a lot of ordinal numbers with even different magnitudes. However, only the invoked fourteenth component with $\hat{B}_{14} = 0.045\,T$ can interact with the rotor part in order to generate a nearby constant mechanical average torque.

IV.   VECTOR CONTROLLED HIGHER HARMONIC AIRGAP-WAVE BASED PERMANENT MAGNET MOTOR

The vector control mode operates the permanent magnet motor like a current source inverter driven machine applying a continuous current modulation [11-13]. Therefore, a very precise knowledge of the rotor position is necessary. This could be managed by applying an encoder on the rotating shaft. The vector control software is adapted to the hardware system which is schematically depicted in Fig.1.

A.   Mathematical motor model

The practical realization of the control structure is fortunately done within the rotor fixed (d,q) reference system, because the electrical stator quantities can there be seen to be constant within the steady operational state [14,15]. The stator voltage and flux linkage space vectors are therefore formulated in the (d,q) rotor reference frame as

$$\underline{u}_{Sdq}(\tau) = r_S \underline{i}_{Sdq}(\tau) + \frac{d\underline{\psi}_{Sdq}(\tau)}{d\tau} + j\omega(\tau)\underline{\psi}_{Sdq} \ , \qquad (2)$$

$$\underline{\psi}_{Sdq}(\tau) = l_S \underline{i}_{Sdq}(\tau) + \underline{\psi}_{Mdq} \ , \qquad (3)$$

whereby r_S denotes the normalized stator resistance and $\omega(\tau)$ stands for the mechanical speed of the shaft. Thereby, the relation (3) covers only weak-saturable isotropic motor designs. The inclusion of some basic identities for the permanent magnet flux space vector in the (d,q) system, namely

$$\frac{d}{d\tau}\underline{\psi}_{Mdq} = 0 \ , \ \underline{\psi}_{Mdq} = \psi_M + j0 \ , \qquad (4)$$

reduces the system (2), (3) to the set of equations

$$u_{Sd}(\tau) = r_S i_{Sd}(\tau) + l_S \frac{d}{d\tau} i_{Sd}(\tau) - \omega l_S i_{Sq}(\tau) \ , \qquad (5)$$

$$u_{Sq}(\tau) = r_S i_{Sq}(\tau) + l_S \frac{d}{d\tau} i_{Sq}(\tau) + \omega l_S i_{Sd}(\tau) + \omega \psi_M \ . \qquad (6)$$

Unfortunately, both equations (5), (6) are always directly coupled without the exception of standstill at $\omega = 0$. That fact is very unsuitable in particular for the design of the current controller. Thus, with regard to the used vector control topology, a more favorable rewritten form of (5), (6) as

$$u_d(\tau) = u_{Sd}(\tau) + \omega l_S i_{Sq}(\tau) =$$

$$= r_S i_{Sd}(\tau) + l_S \frac{d}{d\tau} i_{Sd}(\tau) \qquad , \qquad (7)$$

$$u_q(\tau) = u_{Sq}(\tau) - \omega l_S i_{Sd}(\tau) - \omega \psi_M =$$

$$= r_S i_{Sq}(\tau) + l_S \frac{d}{d\tau} i_{Sq}(\tau) \qquad , \qquad (8)$$

is commonly introduced. The decoupled structure (7), (8) introduces in Fig.6 fortunately both fictive voltages $u_d(\tau)$, $u_q(\tau)$ in order to adjust the controller of both axes independently from each other.

B.   Simplified block diagram of closed-loop control

The control schema in accordance to (7), (8) is realized in Fig.7 with regard to the d- and q- axis notation as a two-step overlaid cascade structure.

The outer speed cascade allows adjusting a pre-set speed value n_{def}, after getting smoothed by a PT1-element. The output of the PI speed controller is also smoothed by a PT1-element and restricted by the thermal I^2t-protection in order to avoid thermal damages. The PI speed controller has a moderate sampling rate and determines the demanded q-current component. The drive is operated with a default zero d-current component in order to achieve maximal torque output. The actual measured electrical phase currents are transformed to the rotor fixed (d,q) reference system and continuously compared to the demanded d and q current components at the innermost current cascade structure. With regard to the d- and q-axis separation, the generated PI-current controller output voltages $u_d(\tau)$, $u_q(\tau)$ are almost seen as fictive quantities in Fig.7, from which the de-coupling-circuit given in Fig.6 calculates the real demanded stator voltage components $u_{Sd}(\tau)$, $u_{Sq}(\tau)$ afterwards. The PI current controller is processed by a rate of 8 kHz.
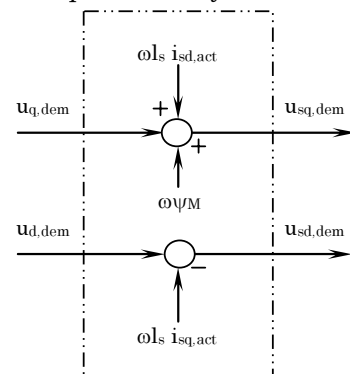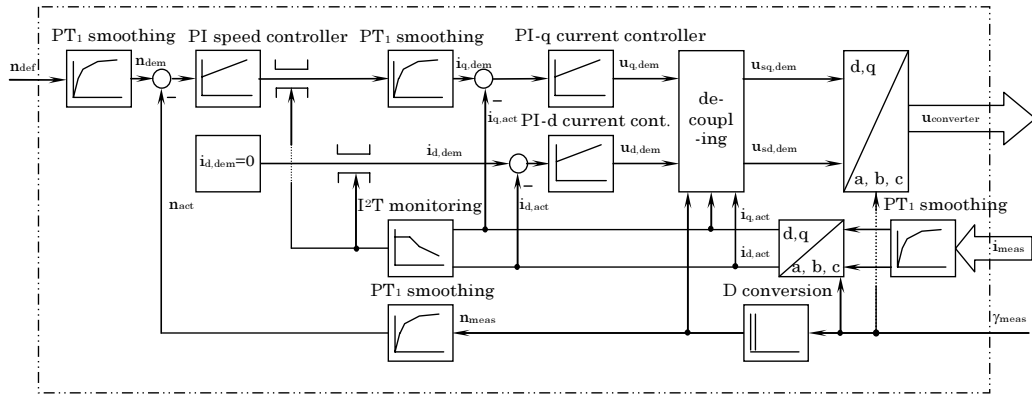

Figure 6. Block diagram of the decoupling-circuit.

Figure 7. Outline of important devices of the vector controlled permanent magnet motor.

C. Electrical current shape and harmonic spectrum

The vector control operation within the quasi-steady operational state at rated-load condition and a default speed value of 400 rpm enforces the time dependent current shape depicted in Fig.8 within the numerical calculation. A direct comparison with the measured course in Fig.9 in real-time conditions shows a very good agreement and confirms the assumptions and simplifications within the numerical analysis procedure. The series expansion

$$i(t) = \sum_{k=1}^{\infty} \hat{I}_k \sin\left(2\pi kf \cdot t + \beta_k\right) \tag{9}$$

of the calculated electrical current from Fig.8 leads the harmonic components $\hat{I}_k$, $k \in \mathbb{N}$. It is obvious from the spectrum in Fig.10, that only the desired fundamental component $\hat{I}_1 = 3.75\text{A}$ at 93.3 Hz is governing the total spectrum. The vector control in conjunction with the special motor obviously avoids additional harmonic components and restricts therefore unexpected thermal heating due to time-harmonic currents.

D. Electromagnetic torque and spectrum

The numerical calculated time-dependent mechanical torque m(t) is depicted in Fig.11. It results from the series expansion in time

$$m(t) = \sum_{k=0}^{\infty} \hat{M}_k \sin\left(2\pi kf \cdot t + \lambda_k\right) \tag{10}$$

that there exists within the harmonic components $\hat{M}_k$, $k \in \mathbb{N}_0$ almost the desired constant contribution of $\hat{M}_0 = 1.3\text{Nm}$. Taking a closer look to the calculated mechanical torque in Fig.12, a very distinct undesired harmonic component $\hat{M}_6 = 0.1\text{Nm}$ known as load pulsation moment exists at 559.8 Hz.
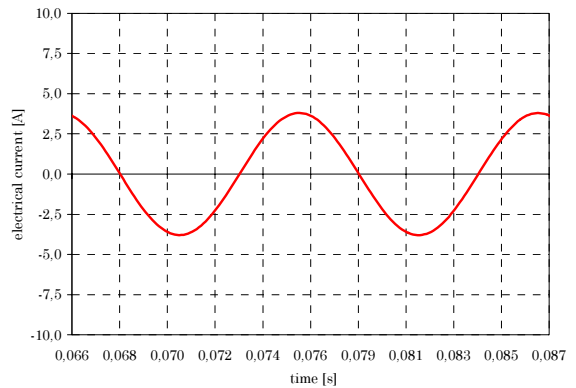

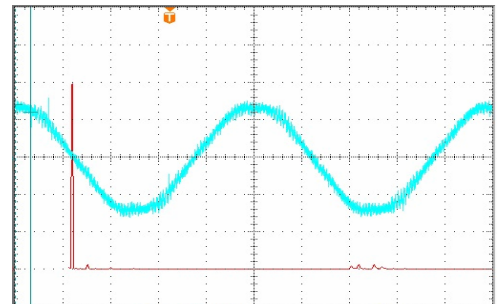Figure 8. Calculated motor current i(t) for a speed range of 400 rpm and a constant load of 1.35 Nm.

Figure 9. Measured motor current i(t) for a speed range of 400 rpm and a constant load of 1.35 Nm. One division corresponds to 2 ms in the abscissa and 2.5 A in the ordinate.
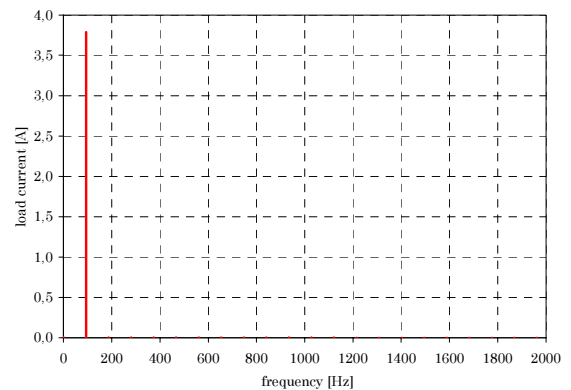

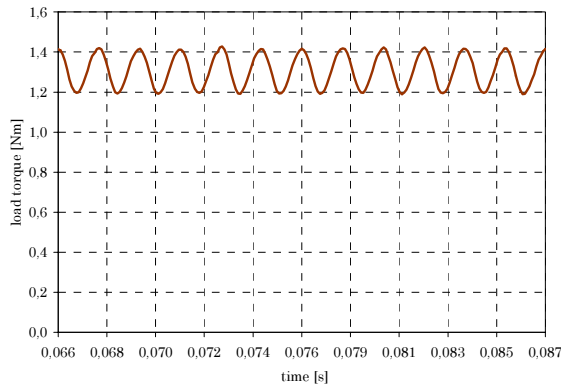Figure 10. Calculated motor current i(t) for a speed range of 400 rpm and a constant load of 1.35 Nm.

Figure 11. Calculated shaft torque m(t) for a speed range of 400 rpm and a constant load of 1.35 Nm.
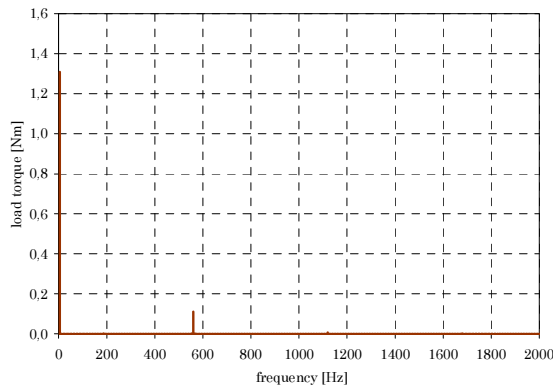

Figure 12. Fourier coefficients $\hat{M}_k$ of the shaft torque for a speed range of 400 rpm and a constant load of 1.35 Nm.

V. BRUSHLESS DC CONTROLLED HIGHER HARMONIC AIR-GAP WAVE BASED PERMANENT MAGNET MOTOR

The brushless DC magnet motor is operated with a space current distribution which does not rotate smoothly but remains fixed in distinct positions within sixty electrical degrees, and jumps suddenly to a position sixty electrical degrees ahead [16].

The brushless DC mode is also known as an electronically commutated motor operation. The current has to be commutated electronically between different phases controlled by diverse switching semiconductors [17,18]. This is possible due to three Hall sensors which provide the necessary six electrical commutation information during the rotor shaft movement. The current magnitude is kept to a required value and the current flows only through two of the three phases coevally.

The generated average mechanical torque remains always constant within the sixty degree electrical periods. The brushless DC control algorithm is set up at the hardware explained in Fig.1.

A. Mathematical motor model

The machine equations in terms of according stator space vector notation is written in a stator fixed reference frame as

$$\underline{u}_{S\alpha\beta}(\tau) = r_S \underline{i}_{S\alpha\beta}(\tau) + \frac{d\underline{\psi}_{S\alpha\beta}(\tau)}{d\tau} \ . \qquad (11)$$

The introduced stator flux space vector in (11) is fortunately written in case of weak-saturable isotropic inductances as

$$\underline{\psi}_{S\alpha\beta}(\tau) = l_S \underline{i}_{S\alpha\beta}(\tau) + \underline{\psi}_{M\alpha\beta} \ , \qquad (12)$$

whereby a rotor flux space vector of constant magnitude is assumed. The governing relation for the brushless DC feature is derived from (11),(12)

$$\underline{u}_{S\alpha\beta}(\tau) = r_S \underline{i}_{S\alpha\beta}(\tau) + l_S \frac{d}{d\tau} \underline{i}_{S\alpha\beta}(\tau) + j\omega \underline{\psi}_{M\alpha\beta} \ , \qquad (13)$$

whereby any transformation into a rotor fixed (d, q) reference system is avoided.

B. Simplified block diagram of the closed-loop brushless DC control

The imported Hall sensor signals, denoted after the interface with γ_{meas}, are transformed to a continuous actual speed value with the aid of a D-element. Due to the low number of six Hall sensors, only very rough speed detection is feasible. The smoothed signal by a PT1 is denoted as n_{act}. The actual speed n_{act} is compared with the demanded speed n_{dem}. The difference is in Fig.13 applied to the moderate PI speed controller which delivers the required motor current magnitude. This value is further limited by the thermal I^2T protection, which takes implicit use of the actual measured motor current i_{act}.

The innermost loop in Fig.13 serves as current control. The actually measured motor current i_{meas} first passes a PT1 smoothing block, before the obtained signal i_{act} is processed with an 8 kHz sampling rate of the current-controller. Depending on the difference between the demanded current magnitudes i_{dem} and the smoothed measured current i_{act}, the necessary motor voltage magnitude u_{dem} is calculated with the aid of a PI current controller.
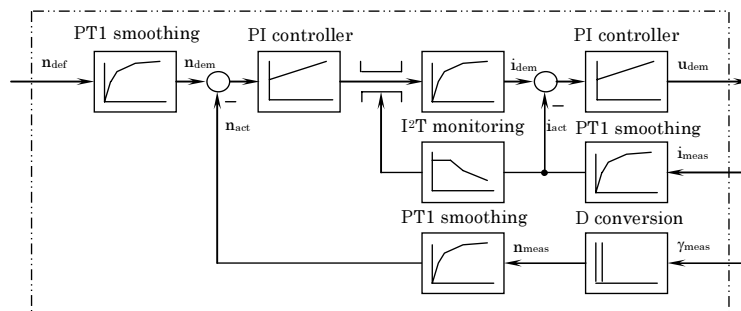
Figure 13. Simplified block diagram of the closed-loop speed and current control.

C. Current shape and harmonic spectrum

The influence of the electrical current commutation from one phase to the other can be clearly seen in the calculated time-dependent course of Fig.14 for rated-load and the speed of 400 rpm. The measured quantity is given in Fig.15. Direct comparison of calculated with measured courses shows a very good concordance. The implemented numerical analysis is also very suitable to predict even higher harmonics in the motor current. The complete current spectrum (9) contains the fundamental component $\hat{I}_1 = 3.84A$ at 93.3 Hz. Moreover, some very distinct peaks within the spectrum could be observed. Several invoked higher harmonics such as $\hat{I}_5 = 0.81A$ at 466.6 Hz, $\hat{I}_7 = 0.62A$ at 653.3 Hz, $\hat{I}_{11} = 0.31A$ at 1026.3 Hz and $\hat{I}_{13} = 0.21A$ at 1212.9 Hz are causing negative effects, such as undesired thermal heating.

D. Electromagnetic torque and spectrum

The numerical calculated time-dependent mechanical torque m(t) is depicted in Fig.17 for rated-load and a speed value of 400 rpm. It results from the series expansion (10) that there exists within the harmonic components $\hat{M}_k$, $k \in \mathbb{N}_0$ almost the desired constant contribution of $\hat{M}_0 = 1.36Nm$. The known undesired torque fluctuations within Fig.17 can be seen more clearly in the harmonic spectrum depicted in Fig.18. Both distinct higher components are found to be $\hat{M}_6 = 0.12Nm$ at 559.8 Hz and $\hat{M}_{12} = 0.09Nm$ at 1119.6 Hz. Other contributions to the torque ripple are obviously suppressed. The occurring undesired load tip effects are well known to be responsible for eventually undesired noise emission.
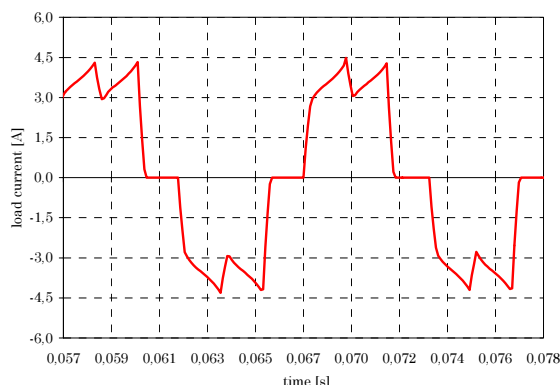

Figure 14. Calculated motor current i(t) for a speed range of 400 rpm and a constant load of 1.35 Nm.

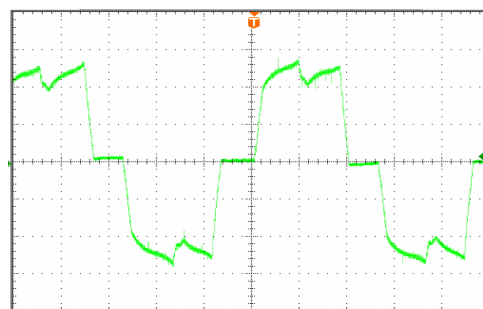

Figure 15. Measured motor current i(t) for a speed range of 400 rpm and a constant load of 1.35 Nm. One division corresponds to 2 ms in the abscissa and 1.5 A in the ordinate.
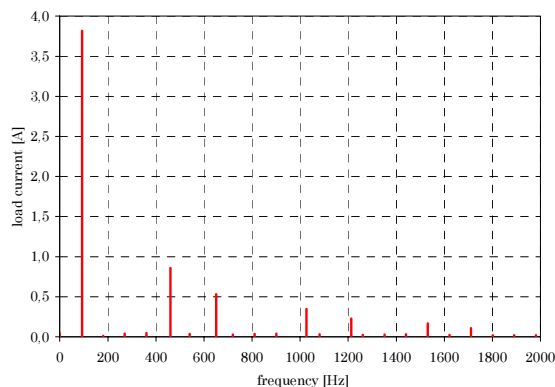

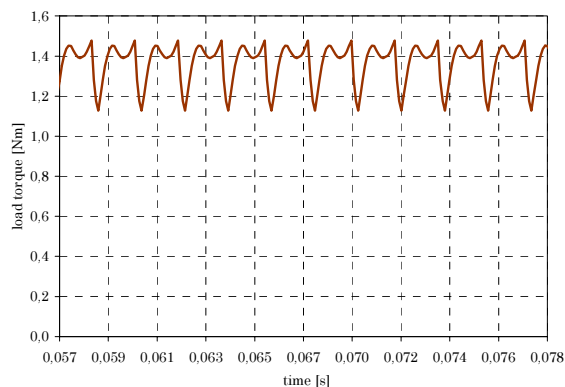Figure 16. Calculated motor current i(t) for a speed range of 400 rpm and a constant load of 1.35 Nm.

Figure 17. Calculated shaft torque m(t) for a speed range of 400 rpm and a constant load of 1.35 Nm.
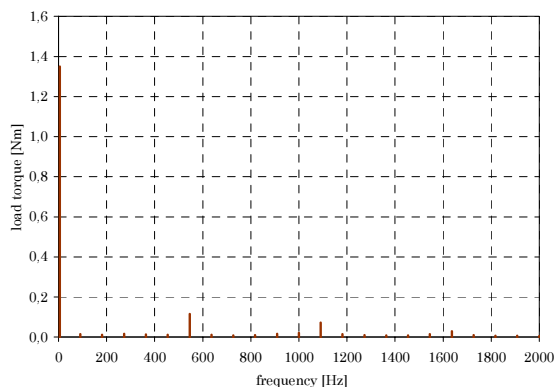

Figure 18. Fourier coefficients $\hat{M}_k$ of the shaft torque for a speed range of 400 rpm and a constant load of 1.35 Nm.

VI. COMPARISON OF BOTH CONTROL METHODS

In case of the well-balanced motor construction and a diligent sensor adjustment, the mostly undesired torque fluctuation of the unskewed motor design still exist within the vector and brushless DC operational mode. In case of some technical applications, this disadvantage could be accepted; otherwise the rotor has to be skewed. However, for many circumstances, the easy unskewed motor construction and the much cheaper brushless DC control mode in conjunction with the higher harmonic airgap wave based motor design is often favorized. Unfortunately, additional copper losses and varying iron losses are still reducing the thermal torque speed characteristic. In order to overcome those circumstances within certain ranges, the vector mode is commonly preferred.

VII. CONCLUSION

The novel axially unskewed higher harmonic airgap wave based permanent magnet motor technology has been analyzed with regard to the closed-loop vector as well as brushless DC control method.

The main focus is thereby given to the verification of previously unknown and almost undesired effects, which could significantly worsen the quality of the complete drive system. The vector control method enforces only one distinct fundamental component in the electrical current consumption, whereas the brushless DC control causes a wide harmonic current spectrum. Undesired load pulsation effects of the unskewed motor could be slightly reduced by preferring the vector control method.

The applied transient electromagnetic-mechanical finite element calculation method with additionally coupled external circuits in the time-domain allows the inclusion of basic control features and is therefore very suitable for a straightforward and accurate analysis of the complete converter fed speed-variable drive system in advance.

REFERENCES

[1] J.S. Salon, *Finite element analysis of electrical machines,* Cambridge University Press: Cambridge, 1996.
[2] M.J. DeBortoli, *Extensions to the finite element method for the electromechanical analysis of electrical machines, PhD Thesis,* Rensselaer Polytechnic Institute, New York, 1992.
[3] J.P.A. Bastos and N. Sadowski, *Electromagnetic modeling by finite element method,* Marcel Dekker: New York/Basel, 2003.
[4] P.F. Brosch, *Moderne Stromrichterantriebe,* Vogel: Würzburg, 1989.
[5] W. Leonhard, *Control of electrical drives,* Springer: Berlin, 2001.
[6] G.K. Dubey, *Fundamentals of electrical drives*, Alpha Science Int.: Pangbourne, 2001.
[7] K.B. Bimal, *Power electronics and variable frequency drives: technology and applications,* IEEE Press: New York, 1996.
[8] K. Heumann, *Principles of power electronics.* Berlin: Springer Verlag, 1986.
[9] G. Seguier and G. Labrique, *Power electronic converters: dc to ac conversion.* Berlin: Springer Verlag, 1989.
[10] T. Bödefeld and H. Sequenz, *Elektrische Maschinen,* Springer: Wien/New York, 1942.
[11] P. Vas, *Vector control of AC machines*, Oxford University Press: Oxford, 1990.
[12] K.G. Bush, *Regelbare Elektroantriebe: Antriebsmethoden, Betriebssicherheit, Instandhaltung*, Verlag Pflaum: München, 1998.
[13] W. Nowotny and T.A. Lipo, *Vector control and dynamics of AC drives,* Clarendon Press: Oxford, 2000.
[14] P. Vas, *Electrical machines and drives: A space-vector theory approach*, Clarendon Press: Oxford, 1996.
[15] P. Vas, *Parameter estimation, condition monitoring, and diagnosis of electrical machines*, Clarendon Press: Oxford, 1993.
[16] R. Lehmann, *Technik der bürstenlosen Servoantriebe,* Elektronik, Vol. 21, 1989.
[17] T.J.E. Miller, *Brushless permanent magnet and reluctance motor drives,* Clarendon Press: Clarendon, 1989.
[18] J.R. Hendershot and T.J.E. Miller, *Design of brushless permanent-magnet motors,* Oxford university press: Oxford, 1994.